Simultaneous 3D depth-to-basement and density-contrast estimates using gravity data and depth control at few points

Cristiano M. Martins[1], Valeria C. F. Barbosa[1], and João B. C. Silva[2]

ABSTRACT

We have developed a gravity-inversion method for simultaneously estimating the 3D basement relief of a sedimentary basin and the parameters defining a presumed parabolic decay of the density contrast with depth in a sedimentary pack, assuming prior knowledge about the basement depth at a few points. The sedimentary pack is approximated by a grid of 3D vertical prisms juxtaposed in both horizontal directions of a right-handed coordinate system. The prisms' thicknesses represent the depths to the basement and are the parameters to be estimated from the gravity data. To estimate the parameters defining the parabolic decay of the density contrast with depth and to produce stable depth-to-basement estimates, we imposed smoothness on the basement depths and proximity between estimated and known depths at boreholes. We applied our method to synthetic data from a simulated complex 3D basement relief with two sedimentary sections having distinct parabolic laws describing the density-contrast variation with depth. The results provide good estimates of the true parameters of the parabolic law of density-contrast decay with depth and of the basement relief. Inverting the gravity data from the onshore and part of the shallow offshore Almada Basin on Brazil's northeastern coast shows good correlation with known structural features.

INTRODUCTION

Most gravity-inversion methods for estimating the basement relief of a sedimentary basin can be grouped into two categories. The first assumes a constant density contrast between the sediments and the basement (Bott, 1960; Oldenburg, 1974; Leão et al., 1996; Barbosa et al., 1997); the second category assumes a density-contrast variation of the sediments with depth, caused by compaction. Several newly developed depth-to-basement inversions of gravity data as-

sume knowledge of a monotonic decrease of density contrast with depth. Some examples of monotonic laws of density variation with depth are exponential law (Cordell, 1973), quadratic law (Rao, 1990; Gallardo-Delgado, 2003), parabolic law (Chakravarthi and Sundararajan, 2004), cubic polynomial law (García-Abdeslem, 2005), and hyperbolic law (Silva et al., 2006).

Parabolic-law methods (e.g., Chakravarthi and Sundararajan, 2007) estimate the regional gravity background and the depth of the 3D basement relief of a sedimentary basin, assuming the density contrast decays with depth according to a parabolic law. Although this method does not minimize a stabilizing functional, it may lead to a reasonable 3D basement relief because of two combined factors. The first factor establishes that the initial guess of the basement depths is computed by assuming that the gravity anomaly at each gravity station is produced by a horizontally infinite slab below the gravity station whose density contrast varies according to a parabolic law. This initial guess follows, semiquantitatively, the basement-relief geometry. The second factor is a combination of implicit hypotheses in the simulated tests. These hypotheses are (1) the basement relief is very simple, (2) the basement depth is shallow, and (3) the decaying rate of the density contrast with depth is low. The first factor represents a geologically meaningful hypothesis; when combined with the second factor, it may lead to a stable solution. However, basements estimated with Chakravarthi and Sundararajan's (2007) method present approximately the same shape of the gravity anomaly scaled by a multiplicative constant.

We present a 3D depth-to-basement gravity inversion assuming a decrease of the density contrast with depth according to a parabolic law. To determine the parameters defining the parabolic decay of the density contrast with depth, we fix these parameters and obtain a stable basement-relief estimate by imposing smoothness on the basement depths and proximity between the estimated and known depths at boreholes. We repeat this procedure for different values of these parameters and select those associated with a basement relief that best honors the borehole information on basement depth. The depth-to-basement estimate is obtained by minimizing a stabilizing functional with a regularization parameter that makes the total objective

function (including the data-misfit measure) a globally convex function. As a result, our method does not depend on the initial guess of basement depths and can be used to estimate a very complex basement relief whose geologic structures cannot be inferred easily just from inspecting the gravity anomaly.

METHODOLOGY

Let's assume a sedimentary basin consisting of homogeneous basement rock and heterogeneous sediments. We assume that the density contrast between the basement and the sediments decreases with the depth z according to a parabolic law (Rao et al., 1994):

$$\Delta\rho(z) = \frac{\Delta\rho_o^3}{(\Delta\rho_o - \alpha z)^2}, \tag{1}$$

where $\Delta\rho_0$ is the density contrast at the ground surface and α is a factor that controls the gradient of the density contrast with depth (expressed in $g/cm^3/km$).

An arbitrary interface is assumed to separate the sedimentary pack from the presumably homogeneous basement. To estimate the relief of this interface, we select a finite region in the x-y space containing the basin's entire upper surface and discretize it along the x- and y-directions into an $mx \times my$ grid of 3D vertical juxtaposed prisms (Figure 1). The top of each prism coincides with the earth's surface, and all prisms have horizontal dimensions equal to dx and dy along the x- and y-directions, respectively. The thicknesses of the M prisms ($M = mx \cdot my$) are the parameters to be estimated from the gravity data. The prisms' thicknesses $p_j, j = 1,\ldots,M$, represent the depths of the sedimentary basement at M discrete points, which are related to the ith vertical component of the gravity anomaly g_i at the ith observation point ($x = x_i, y = y_i$, and $z = z_i$) by the nonlinear relationship

$$g_i = \sum_{j=1}^{M} f_i(p_j, \Delta\rho_o, \alpha), \quad i = 1,\ldots,M. \tag{2}$$
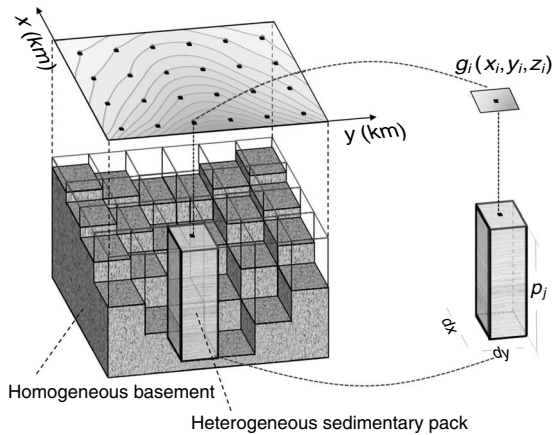

Figure 1. Interpretation model. Gravity anomaly (gray contour lines) interpolated on a regular grid (black dots) produced by a homogeneous basement underlying a sedimentary pack (not shown). The subsurface volume containing the sedimentary pack is discretized into a grid of 3D vertical prisms whose thicknesses are the parameters to be estimated. The inset on the right shows the jth 3D prism and the position (x_i, y_i, z_i) of the ith vertical component of gravity anomaly g_i.

The nonlinear function $f_i(p_j, \Delta\rho_o, \alpha)$ computed at the ith observation point (x_i, y_i, z_i) can be written as

$$f_i = \gamma \int_{xo_j - dx/2}^{xo_j + dx/2} \int_{yo_j - dy/2}^{yo_j + dy/2} \int_{0}^{p_j} \frac{\Delta\rho_o^3}{(\Delta\rho_o - \alpha z_j)^2}$$
$$\cdot \frac{z_i - z'_j}{[(x_i - x'_j)^2 + (y_i - y'_j)^2 + (z_i - z'_j)^2]^{3/2}} dx'_j dy'_j dz'_j, \tag{3}$$

where γ is Newton's gravitational constant and where xo_j and yo_j are the x- and y-coordinates of the jth prism center. Chakravarthi et al. (2002) present a closed form for the integral in equation 3.

We assume that the gravity data are interpolated on a regular grid (Figure 1) whose x- and y-coordinates of each observation point coincide with the respective horizontal coordinates of the prisms' center. The term g_i defines the ith element of vector $\mathbf{g} \equiv (g_1,\ldots,g_M)^T$, which contains the theoretical gravity anomaly caused by M prisms simulating a sedimentary pack whose density contrast decays with depth according to equation 1. The superscript T stands for transposition.

Depth-to-basement inversion

Let $\mathbf{g^o} \equiv (g_1^o, \cdots, g_M^o)^T$ be an M-dimensional vector of gravity observations produced by the basement relief of a sedimentary basin. To obtain unique and stable depth-to-basement estimates at the M discrete points of the $mx \times my$ grid, we look for the solution satisfying the observed gravity anomaly $\mathbf{g^o}$, honoring the borehole information about the basement depth and presenting an overall spatial smoothness on the estimated basement relief. To this end, we formulate a constrained nonlinear inversion to obtain a 3D depth-to-basement estimation by minimizing

$$\|\mathbf{Rp}\|^2 \tag{4}$$

and

$$\sum_{k=1}^{B} \left(\left(\sum_{j=1}^{M} w_{kj}^B p_j \right) - z_k^B \right)^2, \tag{5}$$

subject to

$$\frac{1}{M} \|\mathbf{g^o} - \mathbf{g}(\mathbf{p}, \Delta\rho_0, \alpha)\|^2 = \delta^2 \tag{6}$$

and

$$\mathbf{p} > \mathbf{0}. \tag{7}$$

The values of $\Delta\rho_0$ and α required in equation 6 are obtained through the procedure described in the next section. The first-order Tikhonov regularizing functional (expression 4) (Tikhonov and Arsenin, 1977) imposes a smoothness constraint on the basement relief. In this functional, $\|\cdot\|$ is the Euclidean norm and $\mathbf{R}$ is a matrix representing the first-order discrete differential operator (Twomey, 1963; Vogel, 2002).

The functional in expression 5 introduces borehole information about the depth of the basement by forcing the proximity between the known and estimated depths at the horizontal coordinates of the boreholes. In this functional, B is the number of boreholes that inter-

sect the basement relief at depths z_k^B, $k = 1, \ldots, B$, and w_{kj}^B is the kjth element of a $B \times M$ matrix $\mathbf{W^B}$ whose rows contain only one nonnull element, equal to unity. This nonnull element, located on the kth row of $\mathbf{W^B}$, is associated with the element of vector $\mathbf{p}$, whose corresponding horizontal coordinate is closest to the horizontal coordinates of the kth borehole. In the data-misfit functional (equation 6), $\mathbf{g}(\mathbf{p}, \Delta\rho_o, \alpha)$ is an N-dimensional vector whose ith element contains the computed gravity anomaly at the ith observation point (equation 2) and δ^2 is the expected mean square of the noise realizations in the gravity data.

The constrained inverse problem given by the minimization of functionals 4 and 5, subject to the constraint given by equation 6, can be rewritten as the optimization problem of minimizing the unconstrained functional

$$\frac{1}{M}\|\mathbf{g^o} - \mathbf{g}(\mathbf{p}, \Delta\rho_0, \alpha)\|^2$$
$$+ \mu(\delta)\left[\|\mathbf{Rp}\|^2 + \sum_{k=1}^{B}\left(\left(\sum_{j=1}^{M} w_{kj}^B p_j\right) - z_k^B\right)^2\right], \quad (8)$$

where $\mu(\delta)$ is a nonnegative scalar that controls the trade-off between the data-misfit functional (equation 6) and the prior information (expressions 4 and 5). The minimizer of functional 8 is obtained through Marquardt's (1963) method, incorporating the Gauss-Newton approximation of the Hessian matrix at each iteration (Silva et al., 2001). Finally, the nonnegativity constraint (equation 7) is introduced by a homeomorphic transformation (e.g., Barbosa et al., 1999). However, this constraint can also be introduced via a least-squares algorithm with nonnegativity constraints developed by Haskell and Hanson (1981) (see Silva Dias et al. [2007] for a geophysical example).

Estimating $\Delta\rho_0$ and α

To estimate the basement relief (i.e., to obtain the minimizer $\hat{\mathbf{p}}$ of the unconstrained problem given by equation 8), we first need to obtain estimates of the density contrast at the surface $\Delta\rho_0^*$ and the parabolic decaying factor α^* of the density contrast with depth (equation 1). We get the pair $(\Delta\rho_0^*, \alpha^*)$ in the following way. We fix a pair of values of $\Delta\rho_0$ and α and obtain a vector of parameter estimates $\hat{\mathbf{p}}$ that minimizes the first-order Tikhonov stabilizing functional (expression 4) subject to fitting the gravity observations within the measurement errors (equation 6) and the nonnegativity constraint (equation 7). After estimating vector $\hat{\mathbf{p}}(\Delta\rho_0, \alpha)$, we evaluate the functional

$$\Theta(\Delta\rho_0, \alpha) = \sum_{k=1}^{B}\left(\left(\sum_{j=1}^{M} w_{kj}^B \hat{p}_j(\Delta\rho_0, \alpha)\right) - z_k^B\right)^2, \quad (9)$$

where $\hat{p}_j(\Delta\rho_0, \alpha)$ is the jth estimate of the basement depth for a fixed pair of $\Delta\rho_0$ and α.

Next, we plot $\Theta(\Delta\rho_0, \alpha)$ on the plane $\Delta\rho_0 \times \alpha$. We repeat this procedure for different pairs $(\Delta\rho_0, \alpha)$ to produce a discrete mapping of $\Theta(\Delta\rho_0, \alpha)$ for increments $\Delta\rho_0$ and $\Delta\alpha$ set by the interpreter. The discrete mapping of $\Theta(\Delta\rho_0, \alpha)$ allows a visual estimation of the minimizer $(\Delta\rho_0^*, \alpha^*)$ of $\Theta(\Delta\rho_0, \alpha)$. Then, we check if the inequality

$$\left(\frac{1}{M}\sum_{i=1}^{M}[g_i^o - g_i(\hat{\mathbf{p}}, \Delta\rho_0^*, \alpha^*)]^2\right)^{1/2} \leq L \quad (10)$$

holds. If it does, estimate $\hat{\mathbf{p}}(\Delta\rho_0^*, \alpha*)$ is able to honor the observations within a given threshold L; otherwise, the discretized region $\Delta\rho_0 \times \alpha$ probably does not contain the true pair. In this case, the discretizing grid is refined and the process is repeated.

APPLICATION TO SYNTHETIC DATA

Figure 2a shows the noise-corrupted Bouguer anomaly (solid blue lines) produced by the simulated sedimentary basin with a complex basement relief (Figure 2b). The gravity data were computed on plane $z = 0$ km at the nodes of a 26×78 grid with a grid spacing of 1 km in the x- and y-directions (north-south and east-west, respectively). We corrupted the theoretical anomaly with zero-mean Gaussian pseudorandom noise with a standard deviation of 0.1 mGal.

Figure 2b shows a contour map and a perspective view of the true depths of the basement relief. We assumed that a heterogeneous sedimentary pack overlays a homogeneous basement having a complex structural framework strongly controlled by a sequence of northwest-trending normal faults segmenting the basement relief into a complex mosaic of structural lows and highs separated into two regions (I and II, Figure 2a and b). We assumed that the density contrast decays with depth according to a parabolic law (equation 1). We defined different parabolic laws of density variation with depth to regions I and II by assigning different pairs $(\Delta\rho_0, \alpha)$ to each region $(-0.6$ g/cm^3 and 0.10 g/cm^3/km to region I; -0.4 g/cm^3 and 0.05 g/cm^3/km to region II). Region II is a northwest-elongated subbasin consisting of two isolated, fault-bounded structural lows whose maximum depth attains 7.2 km. In region I, there is a sequence of alternating structural highs and lows close to each other and controlled by northwest-trending faults. The depth to the bottom in this region varies from 3.5 to 7.2 km. The most striking feature of Figure 2a is that neither the existence of two structural lows in region II nor the existence of four structural lows in region I can be inferred easily from the gravity anomaly inspection.

Estimating $\Delta\rho_0$ and α

To estimate the 3D basement relief, we need to know an optimum estimate of the pair $(\Delta\rho_0, \alpha)$ through the discrete mapping of $\Theta(\Delta\rho_0, \alpha)$ (equation 9) for each of the regions I and II in Figure 2. We set an initial interpretation model consisting of a 26×78 grid of 3D vertical prisms in the x- and y-directions, respectively, with the same horizontal dimension, 1.0 km. Next, we define intervals for investigation and increments for $\Delta\rho_0$ and α for regions I and II to produce the discrete mapping of the functional $\Theta(\Delta\rho_0, \alpha)$ (equation 9), shown in Figure 3a; for region I, we use information about the basement depths from three boreholes (black asterisks in Figure 2a).

We note that a wide minimum region (dark gray region in Figure 3a) contains the true $(\Delta\rho_0, \alpha)$ pair (white cross in Figure 3a). All pairs $(\Delta\rho_0, \alpha)$ that lie inside this minimum region are associated with good estimates of the true basement relief, as illustrated by the four estimates of the basement relief (dashed gray lines, Figure 3b), each obtained by using the pairs $(\Delta\rho_0, \alpha)$ at points 1–4 (white dots and white cross, Figure 3a). These pairs yield an acceptable anomaly fit (mean error ≈ 0.08 mGal).

In region II, we produced two discrete mappings of the functional $\Theta(\Delta\rho_0, \alpha)$ on the plane $\Delta\rho_0 \times \alpha$. The first one (Figure 4a) uses information about the basement depths from seven boreholes (blue asterisks in Figure 2a). Although the number of boreholes is high, the minimum region of the functional $\Theta(\Delta\rho_0, \alpha)$ is not well defined and
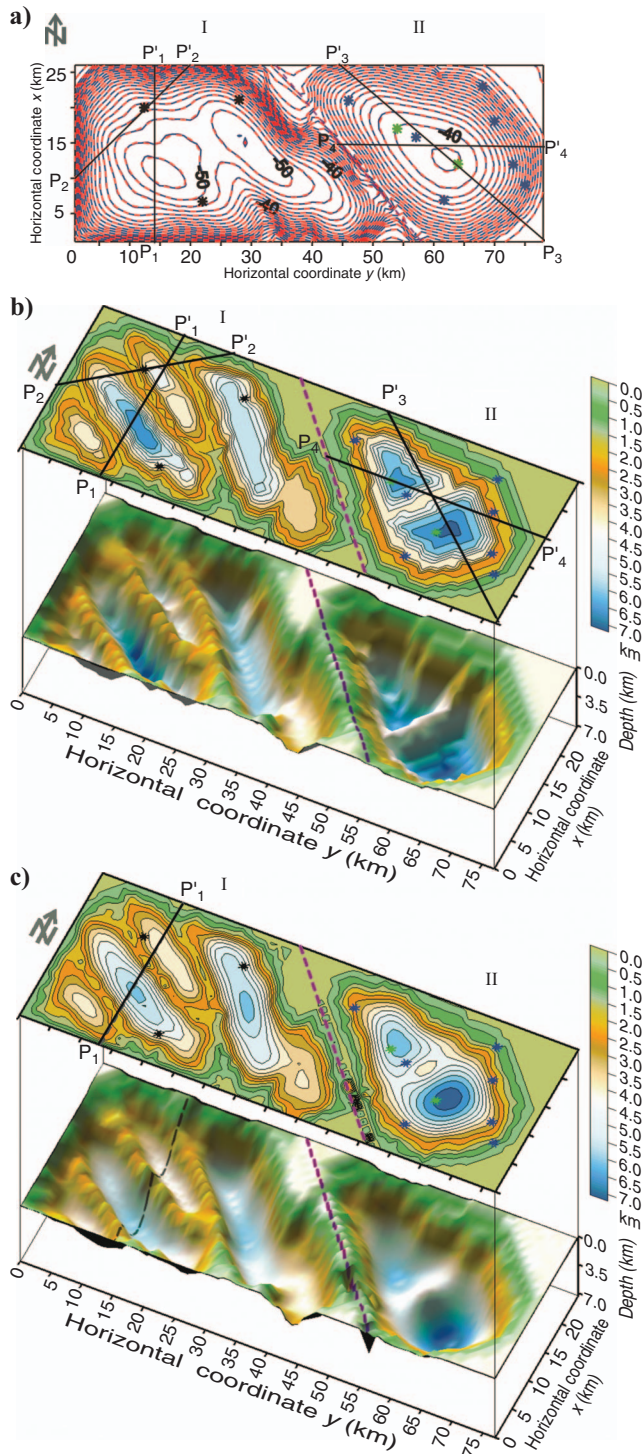
a)

b)

c)

Figure 2. Synthetic test. (a) Noise-corrupted Bouguer anomaly (solid blue lines) produced by the simulated basement relief shown in (b). Fitted Bouguer anomaly (dashed red lines) is produced by the estimated basement relief shown in (c). (b) Contour map and perspective view of the simulated basement relief, which is divided into two regions (I and II) with different parabolic laws of density variation with depth: ($\Delta\rho_0 = -0.6$ g/cm^3, $\alpha = 0.10$ g/cm^3/km) for region I and ($\Delta\rho_0 = -0.4$ g/cm^3, $\alpha = 0.05$ g/cm^3/km) for region II. (c) Contour map and perspective view of the estimated basement depth. The line segments P$_1$-P$'_1$ through P$_4$-P$'_4$ indicate the locations of the profiles shown in Figures 3b, 5, and 6. The asterisks indicate the borehole locations used to estimate $\Delta\rho_0$ and α.

does not contain the true pair ($\Delta\rho_0, \alpha$) (white cross in Figure 4a). The second discrete mapping of $\Theta(\Delta\rho_0, \alpha)$ (Figure 4b) uses information about the basement depths on region II provided by nine boreholes (blue and green asterisks in Figure 2a). Conversely, in this second case, the borehole information is sufficient to yield a well-defined minimum region of $\Theta(\Delta\rho_0, \alpha)$ containing the true pair ($\Delta\rho_0, \alpha$) (white cross in Figure 4b). In addition, the pair located at the minimum of $\Theta(\Delta\rho_0, \alpha)$ yields an acceptable anomaly fit (mean error ≈ 0.15 mGal).

These results show that the minimum region of the functional $\Theta(\Delta\rho_0, \alpha)$ (equation 9) may not include the true pair ($\Delta\rho_0, \alpha$). Inclusion depends on the number and distribution of boreholes and on the gravity response. Later in this article, we address the number of boreholes necessary to obtain the true pair ($\Delta\rho_0, \alpha$), validated semi-quantitatively through spectral analysis.

Estimating 3D basement relief

Figure 2c shows a contour map and a perspective view of the estimated depths of the basement relief using estimated values of $\Delta\rho_0$ and α obtained for regions I and II (Figure 2a) by performing a systematic search of the functional $\Theta(\Delta\rho_0, \alpha)$ and checking if inequali-
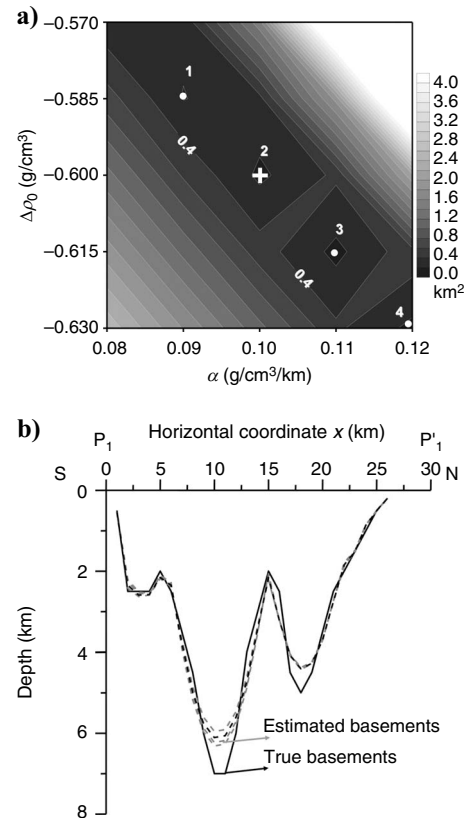
a)

b)

Figure 3. Synthetic test, region I. (a) Contour map of functional $\Theta(\Delta\rho_0, \alpha)$ (equation 9) using three boreholes (black asterisks in Figure 2a) on plane $\Delta\rho_0 \times \alpha$, showing the minimum region (black). The white cross indicates the estimated pair ($\Delta\rho_0, \alpha$), which coincides with the true one. The pairs ($\Delta\rho_0, \alpha$) at points 1–4 lie inside the broad minimum region of $\Theta(\Delta\rho_0, \alpha)$. (b) True (solid black line) and estimated (dashed gray lines) basement reliefs along the profile P$_1$-P$'_1$ whose location is shown in Figure 2c, using the pairs ($\Delta\rho_0, \alpha$) at points 1–4 shown in (a).

ty 10, which defines a possible ambiguity region, holds. We use the pair ($\Delta\rho_0^* = -0.6$ g/cm³, $\alpha^* = 0.10$ g/cm³/km) inside the minimum of $\Theta(\Delta\rho_0, \alpha)$ (Figure 3a), which fits the data with a mean error of about 0.08 mGal. For region II, we use the pair ($\Delta\rho_0^* = -0.4$ g/cm³, $\alpha^* = 0.05$ g/cm³/km) inside the minimum of $\Theta(\Delta\rho_0, \alpha)$ (Figure 4b), which fits the data with a mean error of about 0.15 mGal. By comparing the basement-depth estimates (Figure 2c) with the true depths (Figure 2b), we certify the good performance of our method in recovering a complex basement relief. The corresponding fitted anomaly is displayed in Figure 2a (red dashed line).

Our method can be modified to estimate the basement of a sedimentary basin presenting a discontinuous relief such as the method proposed by Barbosa et al. (1999). It also can be used in basinlike features with smaller dimensions than a sedimentary basin, such as waste landfills (Silva et al., 2009).

Spectral analysis

We have found that region I requires less basement-depth information from a borehole than region II to estimate the true pair ($\Delta\rho_0, \alpha$) correctly. We interpret this difference as a greater resolution degradation of the gravity anomaly with respect to the basement relief in region II relative to region I.

In this section, we perform spectral analysis to support this interpretation. To this end, we compute, in the wavenumber domain k, the amplitude spectra of the noise-free gravity anomaly $|A_g(k)|$ and of the true basement relief $|A_h(k)|$ along profiles P_1-P_1' through P_4-P_4'

(Figure 2a). Then we compute for each profile the Euclidean norm $\|\cdot\|_2$ of the difference between $|A_g(k)|$ and $|A_h(k)|$, i.e.,

$$c = \||A_g(k)| - |A_h(k)|\|_2. \tag{11}$$

The coefficient c assesses, semiquantitatively, the loss in the high-frequency content of the gravity anomaly relative to the basement relief. The smaller the value of c, the smaller the resolution loss of the gravity anomaly and the fewer the number of boreholes required to obtain the true pair ($\Delta\rho_0, \alpha$).

Figures 5 and 6 show the noise-free gravity and the basement-relief profiles across regions I and II, respectively. Table 1 shows the values c for these profiles. The values of this coefficient for the profiles across region I are about twice as small as the values obtained for profiles across region II, confirming the smaller resolution degradation of the gravity anomaly relative to the basement relief in region I as compared with region II and the consequent need for fewer boreholes to obtain the true pair ($\Delta\rho_0, \alpha$) in region I as compared with region II.

In this synthetic example, spectral analysis answers the question, "Why does a complex basement relief (such as region I, Figure 2b) require fewer known basement depths than a simple basement relief (such as region II, Figure 2b) to estimate the true pair ($\Delta\rho_0, \alpha$) correctly?" This analysis evidently cannot be extended to a real case because it assumes knowledge of the entire basement relief.

APPLICATION TO REAL DATA

We evaluate the performance of our method by applying it to a gravity data set from onshore and part of the shallow offshore Almada Basin on Brazil's northeastern coast. The Almada Basin is part of the rift system formed during the Early Cretaceous break-up of South America and Africa, which developed the Brazilian eastern marginal basins (Barbosa et al., 2007). The Almada tectonic frame-
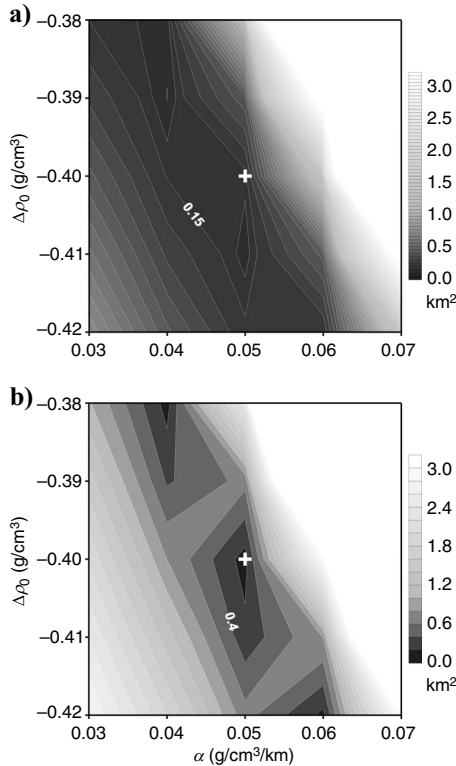

Figure 4. Synthetic test, region II. (a) Contour maps of functional $\Theta(\Delta\rho_0, \alpha)$ (equation 9) on plane $\Delta\rho_0 \times \alpha$ using seven boreholes, displayed as blue asterisks in Figure 2a, and (b) nine boreholes, displayed as blue and green asterisks in Figure 2a. The minimum region of functional $\Theta(\Delta\rho_0, \alpha)$ is the black area. The white crosses indicate the true pair ($\Delta\rho_0, \alpha$).
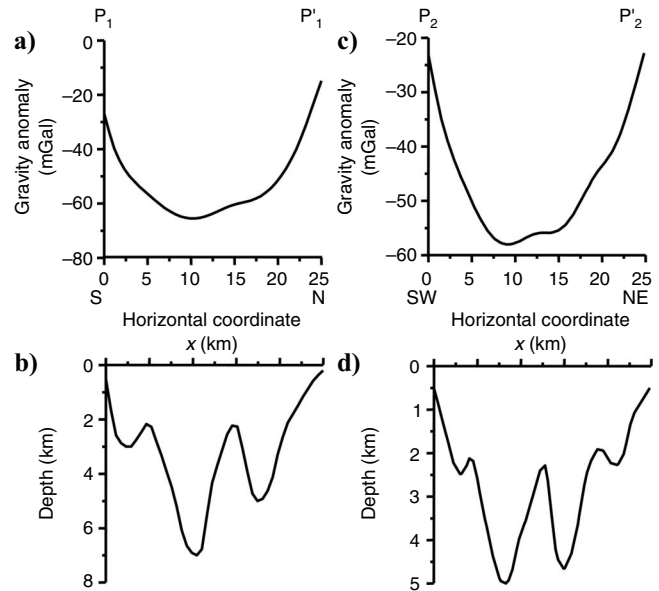

Figure 5. Synthetic test, profiles across region I. (a) Noise-free gravity data and (b) true basement relief along profile P_1-P_1'. (c) Noise-free gravity data and (d) true basement relief along profile P_2-P_2'. The locations of the profiles are shown in Figure 2.

work is made up of horsts and grabens bounded by north-northeast-trending normal faults.

The tectonic-sedimentary evolution of the Almada Basin includes three main stages: prerift, rift, and postrift (Gonçalves et al., 2000). The prerift stage is composed of a sequence of continental sediments made up of fluvial/lacustrine shales and siliciclastic and fluvial/aeolian sandstones. The rift stage is characterized by intense subsidence, resulting in the deposition of a thick succession of pelitic lacustrine deposits — shales with interbedded sandstones and minor limestone, dolomite, and marl layers. The postrift stage includes the transitional and marine phases. The transitional phase is composed of fine-grained sandstones and evaporitic deposits. The marine phase consists of shallow carbonates, fine-grained sandstones, and calcareous mudstones of the shelf-slope marine system. This phase has progradational sequences with the coarse-grained sandstones, platform carbonates, and turbidites of the Urucutuca Formation, which are considered the main reservoir rocks in the Camamu and Almada basins (Milani et al., 2000). Petroleum accumulations in the Camamu-Almada Basin are associated with structural or structural-stratigraphic trapping within prerift and rift reservoirs. In the prerift oil field, petroleum is trapped in the fluvial and aeolian sandstones and the seal is the basement faults. The basement rocks of Almada are mainly made up of Precambrian rocks of the Atlantic granulitic belt.
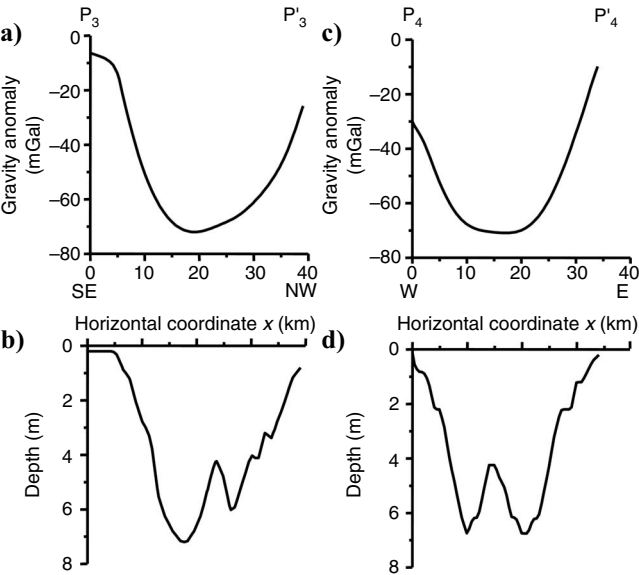

Figure 6. Synthetic test, profiles across region II. (a) Noise-free gravity data and (b) true basement relief along profile P_3-P'_3. (c) Noise-free gravity data and (d) true basement relief along profile P_4-P'_4. The locations of the profiles are shown in Figures 2.

Table 1. The computed coefficients c (equation 11) for each profile P_1-P'_1−P_4-P'_4 (shown in Figure 2b).

Profiles	c
P_1-P'_1	3,944.250
P_2-P'_2	4,358.194
P_3-P'_3	8,581.141
P_4-P'_4	10,276.730

Figure 7 shows the Bouguer anomaly map over the study area, corrected for gravity effects produced by the seawater layer and the crust-mantle interface. The original data (not shown) were corrected for the effect of the seawater layer by subtracting the vertical component of the gravity field produced by the volume of the seawater layer with a density of 1.03 g/cm^3. Next, the effect of deep crustal sources was removed by fitting the original observations by a second-degree polynomial using a robust method (Beltrão et al., 1991) and removing it from the observations.

To estimate the 3D Almada basement relief, we assumed a parabolic law of density variation with depth (equation 1). Even though this assumption allows a density-contrast decay with depth, it does not exclude the possibility of assuming a constant density contrast if α (equation 1) is a small positive number. To apply our depth-to-basement inversion, we first need to know the parameters of the parabolic decay of the density contrast with depth, i.e., to obtain an optimum estimate for ($\Delta\rho_0, \alpha$).

To estimate an optimum pair ($\Delta\rho_0, \alpha$), we produce a discrete and systematic search for $\Delta\rho_0$ and α by using the gravity data and the information about the basement depth from eight boreholes (black asterisks, Figure 7) that touched the Almada's basement relief. We assume, on geologic grounds, that the variation of $\Delta\rho_0$ and α along the north-south direction is negligible and that along the east-west direction only the variation of α is nonnegligible. Hence, we assume that the density contrast at the surface $\Delta\rho_0$ is constant on the onshore or the shallow offshore portions of the Almada Basin.

In this way, we divided the Almada Basin into three distinct regions (Figure 7). Region I is the westernmost portion, and it comprises the onshore portion of the Almada Basin. Region III is the easternmost portion; it comprises the shallower offshore portion of the basin. Region II is a transition zone that contains the coastline.

To estimate optimum ($\Delta\rho_0, \alpha$) for the outermost regions I and III of the Almada Basin, we set an initial interpretation model consisting of a grid of 3D vertical prisms with the same horizontal dimen-
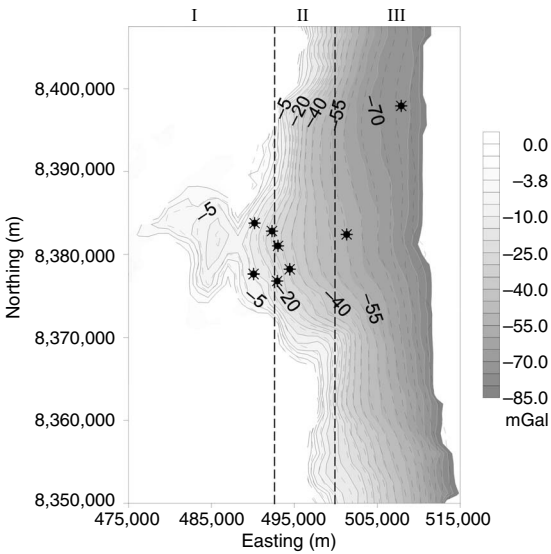

Figure 7. Real test. Bouguer anomaly map from the onshore and a portion of the shallower offshore Almada Basin corrected for the Moho effect. The dashed gray lines show the fitted Bouguer anomaly produced by the corresponding estimated basement relief in Figure 9. The asterisks stand for eight boreholes that touched the basement. Regions I, II, and III are assumed to have different values of α.

sion, 1.2 km. This interpretation model encloses one of the outermost regions (I or III) and the intermediate region II. Next, we define intervals and increments for $\Delta\rho_0$ and α for each region, and we produce two discrete mappings: (1) the projection of the ambiguity region (equation 10) and (2) the functional $\Theta(\Delta\rho_0,\alpha)$ (equation 9). The gravity data and the information about the basement depths from boreholes that touch the Almada's basement relief of region II are included in the discrete and systematic search for optimum $(\Delta\rho_0,\alpha)$ in regions I and III to create an overlap of the gravity data sets and of the boreholes between the combined regions I-II and III-II.

The discrete mappings of the functional $\Theta(\Delta\rho_0,\alpha)$ on the plane $\Delta\rho_0 \times \alpha$ associated with the combined regions I-II and III-II are shown in Figure 8. In both cases, all pairs $(\Delta\rho_0,\alpha)$ lying within the minimum regions (the black strip in Figure 8a and b) yield acceptable anomaly fits, displaying a mean error of 3.4 mGal. For regions I-II and III-II, the optimum estimated $(\Delta\rho_0,\alpha)$ are, respectively, $(\Delta\rho_0 = -0.57$ g/cm³, $\alpha = 0.045$ g/cm³/km) and $(\Delta\rho_0 = -0.57$ g/cm³, $\alpha = 0.050$ g/cm³/km) (white dots, Figure 8a and b). The estimated values of $\Delta\rho_0$ and α for regions I-II and III-II were used in regions I and III, respectively. For region II, we used $\Delta\rho_0 = -0.57$ g/cm³ and an interpolated value of α, given by

$$\alpha_i = \alpha_I + \frac{(\alpha_{III} - \alpha_I)(y_i - y_I)}{y_{II} - y_I}, \qquad (12)$$

where α_i is the value of the parameter α assigned to the ith prism of the interpretation model located in region II, $\alpha_I = 0.045$ g/cm³/km,

$\alpha_{III} = 0.050$ g/cm³/km, y_i is the y-coordinate of the ith prism, and y_I and y_{II} are the y-coordinates (easting coordinates) of the limits between regions I and II and regions II and III, respectively.

Figure 9 shows the depth-to-basement estimates of the study area, which fits the observed gravity data (dashed gray lines in Figure 7). We used an interpretation model composed of a grid of 3D vertical prisms with the same x- and y-dimensions of 1.2 km. The top of the prisms coincide with the bathymetric depth in the offshore portion of the sedimentary basin, so the lower limit of the integration of variable z' in equation 3 is not zero. On the other hand, in the onshore portion, the top of the prisms coincides with the earth's surface; then the lower limit of the integration of z' in equation 3 is zero because this portion is located at low altitude and a relatively flat area near sea level. To avoid edge effects, we extend the data and interpretation model beyond the easternmost, northernmost, and southernmost limits of the gravity data. This extension covers about 12 km along each of the three directions. For the entire basin, the constant value assigned to $\Delta\rho_0$ is -0.57 g/cm³. In region II, the variation of α along the east-west direction follows equation 12. In regions I and III, the constant values assigned to α are 0.045 and 0.050 g/cm³/km, respectively.

The estimated relief is not just a scaled version of the gravity anomaly. Rather, it presents several features that are not apparent in the Bouguer anomaly map of Figure 7. First, the estimated relief presents steep borders, evidencing the presence of gravity faults (white lines in Figure 9). Also, we note the existence of terraces A, B, and C separating two local subbasins (D and E). These features are important in understanding the basin evolution and in detecting structural oil traps. Table 2 lists the observed and estimated basement depths at the eight boreholes.
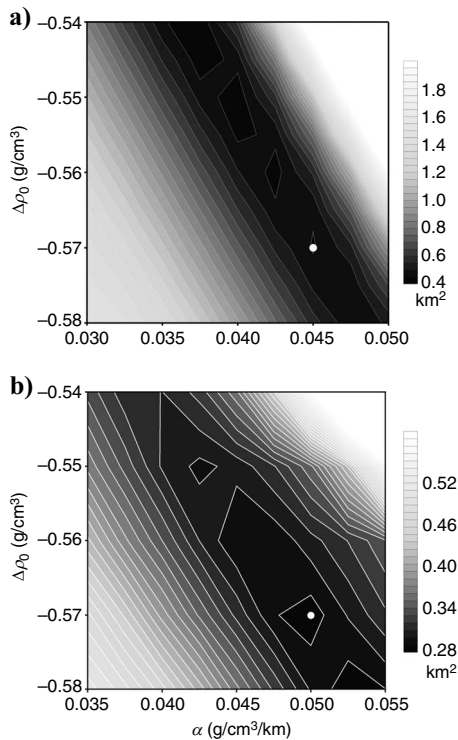

Figure 8. Real test. (a) Functional $\Theta(\Delta\rho_0,\alpha)$ (equation 9) on plane $\Delta\rho_0 \times \alpha$, showing the minimum regions (black) of the combined regions: (a) I–II; (b) III–II. The white dots indicate the estimated pairs $(\Delta\rho_0,\alpha)$.
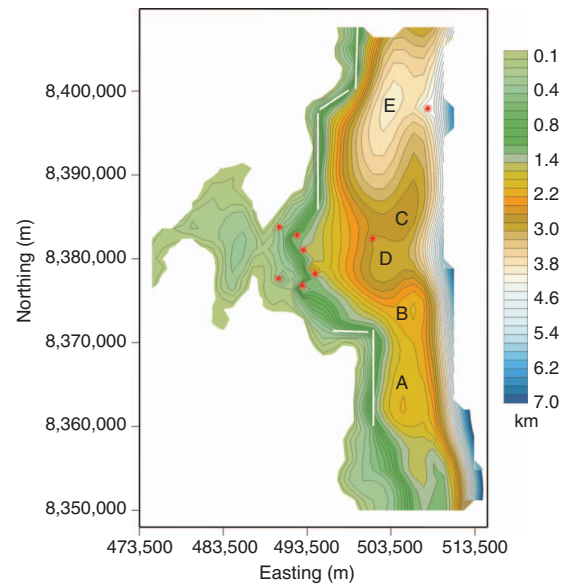

Figure 9. Real test. Estimated basement depth of the onshore and a portion of the shallower offshore Almada Basin. The white lines highlight the steep basin borders, probably associated with gravity faults. A, B, and C locate terraces that are structural highs; D and E indicate subbasins.

Table 2. Coordinates of boreholes and the corresponding observed, estimated, and residual (absolute differences between observed and estimated) basement depths to the real test.

Northing coordinate	Easting coordinate	Observed (km)	Estimated (km)	Residual (km)
8,383,600	490,600	0.381	0.420	0.039
8,377,600	490,600	0.453	0.463	0.010
8,382,400	491,800	1.171	1.147	0.024
8,381,200	493,000	1.427	1.411	0.016
8,376,400	493,000	1.597	1.546	0.051
8,378,800	494,200	2.182	2.140	0.042
8,382,400	501,400	2.875	2.867	0.008
8,398,000	507,400	4.272	4.256	0.016

CONCLUSIONS

The impossibility of determining the density and volume of a source from gravity data only is well known and follows directly from Newton's law of gravitation. Here, we used depth-to-basement information at a few points to estimate simultaneously the 3D basement relief (volume of the source) and parameters defining a presumed parabolic decay of the density contrast with depth in a sedimentary basin. Hence, we used knowledge about the source's volume at a few points to overcome the fundamental ambiguity involving the product of the physical property by the volume. Our synthetic data examples show that the method produces good estimates of the sedimentary basement relief, even in the case of a complex geologic setting. The estimated relief is not just a scaled version of the observed gravity anomaly. Rather, it contains features disclosed by the inversion process. In addition, this method estimates the density contrast at the surface and the decaying factor of the density contrast with depth. The validity of this estimation procedure has been confirmed in tests with synthetic data and in the case of real data from the Almada Basin. The method may be modified to estimate the basement relief of a faulted extensional sedimentary basin and the buried landfill bottom topography.

ACKNOWLEDGMENTS

REFERENCES

Barbosa, V. C. F., P. T. L. Menezes, and J. B. C. Silva, 2007, Gravity data as a tool for detecting faults: In-depth enhancement of subtle Almada's basement faults, Brazil: Geophysics, **72**, no. 3, B59–B68.

Barbosa, V. C. F., J. B. C. Silva, and W. E. Medeiros, 1997, Gravity inversion of basement relief using approximate equality constraints on depths: Geophysics, **62**, 1745–1757.

——, 1999, Gravity inversion of a discontinuous relief stabilized by weighted smoothness constraints on depth: Geophysics, **64**, 1429–1437.

Beltrão, J. F., J. B. C. Silva, and J. C. Costa, 1991, Robust polynomial fitting for regional gravity estimation: Geophysics, **56**, 80–89.

Bott, M. H. P., 1960, The use of rapid digital computing methods for direct gravity interpretation of sedimentary basins: Geophysical Journal of the Royal Astronomical Society, **3**, 63–67.

Chakravarthi, V., H. M. Raghuram, and S. B. Singh, 2002, 3D forward gravity modeling of density interfaces above which the density contrast varies continuously with depth: Computers and Geosciences, **28**, 53–57.

Chakravarthi, V., and N. Sundararajan, 2004, Ridge regression algorithm for gravity inversion of fault structures with variable density: Geophysics, **69**, 1394–1404.

——, 2007, 3D gravity inversion of basement relief — A depth-dependent density approach: Geophysics, **72**, no. 2, I23–I32.

Cordell, L., 1973, Gravity analysis using an exponential density-depth function — San Jacinto graben, California: Geophysics, **38**, 684–690.

Gallardo-Delgado, L. A., M. A. Pérez-Flores, and E. Gómez-Treviño, 2003, A versatile algorithm for joint 3D inversion of gravity and magnetic data: Geophysics, **68**, 949–959.

García-Abdeslem, J., 2005, The gravitational attraction of a right rectangular prism with density varying with depth following a cubic polynomial: Geophysics, **70**, no. 6, J39–J42.

Gonçalves, F. T. T., R. P. Bedregal, L. F. C. Coutinho, and M. R. Mello, 2000, Petroleum system of the Camamu-Almada Basin: A quantitative modeling approach, *in* M. R. Mello and B. J. Katz, eds., Petroleum systems of South Atlantic margins: AAPG Memoir 73, 257–271.

Haskell, K. H., and R. J. Hanson, 1981, An algorithm for linear least squares problems with equality and nonnegativity constraints: Mathematical Programming, **21**, 98–118.

Leão, J. W. D., P. T. L. Menezes, J. F. Beltrão, and J. B. C. Silva, 1996, Gravity inversion of basement relief constrained by the knowledge of depth at isolated points: Geophysics, **61**, 1702–1714.

Marquardt, D. W., 1963, An algorithm for least-squares estimation of nonlinear parameters: SIAM Journal, **2**, 601–612.

Milani, E. J., J. A. S. Brandão, P. V. Zalan, and L. A. P. Gamboa, 2000, Petroleum in the Brazilian continental margin — Geology, exploration, results and perspectives: Revista Brasileira de Geofísica, **18**, 352–396.

Oldenburg, D. W., 1974, The inversion and interpretation of gravity anomalies: Geophysics, **39**, 526–536.

Rao, D. B., 1990, Analysis of gravity anomalies of sedimentary basins by an asymmetrical trapezoidal model with quadratic density function: Geophysics, **55**, 226–231.

Rao, V., C. V. Chakravarthi, and M. L. Raju, 1994, Forward modelling: Gravity anomalies of two-dimensional bodies of arbitrary shape with hyperbolic and parabolic density functions: Computers and Geosciences, **20**, 873–880.

Silva, J. B. C., D. C. L. Costa, and V. C. F. Barbosa, 2006, Gravity inversion of basement relief and estimation of density contrast variation with depth: Geophysics, **71**, no. 5, J51–J58.

Silva, J. B. C., W. E. Medeiros, and V. C. F. Barbosa, 2001, Pitfalls in nonlinear inversion: Pure and Applied Geophysics, **158**, 945–964.

Silva, J. B. C., W. A. Teixeira, and V. C. F. Barbosa, 2009, Gravity data as a tool for landfill study: Environmental Geology, **57**, 749–757.

Silva Dias, F. J. S., V. C. F. Barbosa, and J. B. C. Silva, 2007, 2D gravity inversion of a complex interface in the presence of interfering sources: Geophysics, **72**, no. 2, I13–I22.

Tikhonov, A. N., and V. Y. Arsenin, 1977, Solutions of ill-posed problems: W. H. Winston and Sons.

Twomey, S., 1963, On the numerical solution of Fredholm integral equations of the first kind by the inversion of the linear system produced by quadrature: Journal of the Association for Computing Machinery, **10**, 97–101.

Vogel, C. R., 2002, Computational methods for inverse problems: SIAM.